Liu *et al.*
Chinese Journal of Mechanical Engineering (2024) 37:34
https://doi.org/10.1186/s10033-024-01017-5

Chinese Journal of Mechanical Engineering

ORIGINAL ARTICLE

Open Access

Characterization and Analysis of Inconel 718 Alloy Ground at Different Speeds

Hao Liu[1], Huili Han[1], Qinghong Jiang[1,2], Minglin He[1] and Bi Zhang[1*]

Abstract

Inconel 718 (IN718) alloy is widely applied to fabricate high temperature resistant or corrosion resistant parts due to its excellent mechanical performance. However, the machining of IN718 alloy is difficult as it may cause serious tool wear and poor surface quality (SQ) of the workpiece. In this work, grinding experiments on IN718 alloy at different speeds were conducted by using a CBN grinding wheel. The relationship between grinding speed, SQ and subsurface damage (SSD) was well studied. With increasing grinding speed, surface roughness decreased, and SQ was greatly improved. Meanwhile, the microhardness of the grinding surface declined as the grinding speed increased. The SSD depth was almost unchanged when the grinding speed was lower than 15 m/s, then it decreased with higher grinding speeds. It was attributed to the mechanical-thermal synergistic effect in the grinding process. The results indicated that increasing grinding speed can effectively improve the SQ and reduce the SSD of IN718 alloy. The conclusion in the work may also provide insight into processing other hard-to-machining materials.

Keywords Surface integrity, Grinding speed, IN718 alloy, Precision machining, CBN grinding wheel

1 Introduction

IN718 alloy has characteristics of high strength, oxidation resistance, corrosion resistance and excellent fatigue resistance at high temperatures, which is widely used in the field of aerospace, nuclear and petrochemical industry [1, 2]. In spite of the excellent mechanical properties, it has poor thermal conductivity, serious work hardening, high shear strength, variety of hard points (carbides, nitrides and δ strengthening phase), and high chemical affinity for many tool materials [3]. These drawbacks may lead to serious tool wear during machining and poor surface quality (SQ), which obviously increases the processing cost and deteriorates the service performance [4–7]. To solve the difficulty in machining IN718 alloy, many processing techniques have been developed. Kim et al. [8] suggested that it can improve tool life, reduce cutting force and improve material removal rate of IN718 by adopting laser-assisted machining. Moon et al. [9] demonstrated that plasma enhanced machining can improve the machinability of IN718 by alleviating work hardening. However, the thermal effects induced by these processing techniques bring a more serious subsurface damage (SSD) than that processed by conventional machining methods. Ultrasonic vibration machining can also achieve a better SQ and a higher tool life compared with conventional machining, but the machining efficiency is low [10, 11]. In addition, to solve the problem of the low thermal conductivity of IN718, some new cooling lubrication methods such as high-pressure jet coolant assistance and cryogenic machining were applied to take away the heat generated during processing, so as to improve the cooling and lubrication environment and the quality of processed surface [12–15]. The SQ could also be improved by using ceramic tools such as cubic boron nitride (CBN) and coated tools to overcome the characteristics of severe work hardening and many hard points of this material. However, the thermal conductivity of

*Correspondence:
Bi Zhang
zhangb@sustech.edu.cn
[1] Department of Mechanical and Energy Engineering, Southern University of Science and Technology, Shenzhen 518055, China
[2] Department of Mechanical Engineering, Hong Kong Polytechnic University, Hong Kong, China

ceramics tools is low, and heat cannot be dissipated in time during mechanical processing, thus tool wear is still severe [16, 17].

To improve processing efficiency and quality simultaneously, high-speed machining (HSM) technology has attracted lots of attention. Yang and Zhang [18] indicated that material embrittlement and fragmentation occur when loading at a high strain rate. Under HSM, the material is in a high strain rate environment, which leads to the increase in brittleness, and the 'skin effect' of damage can be obtained [19]. Guo et al. [20, 21] carried out high-speed grinding on SiC particle reinforced Al metal matrix composites and Al6061T6 alloy, showing that better SQ and less SSD can be obtained by increasing the grinding speed. Meanwhile, the influence of different components on the machining effect can be alleviated for the composites. Of course, for IN718 alloy, some scholars have studied the effect of machining speed on SQ through machining methods such as turning, milling and drilling [22–25]. However, compared with grinding, the surface quality obtained by these processing methods is relatively poor, and the processing speed is relatively low.

In the current research on improving the machinability of IN718 by high-speed grinding, Dai et al. [26] studied the influence of grinding wheel speed (20–140 m/s) on grinding temperature and power consumption during processing IN718 alloy. They indicated that a grinding speed of 120 m/s could achieve the minimum grinding forces and specific grinding energy, meanwhile, the grinding temperature was lower than 100 °C and surface roughness was lower than 0.3 μm at this speed. Ruzzi et al. [27] showed that increasing the speed of the grinding wheel can improve the surface finish, although the grinding force and friction coefficient are increased when the wheel speed at 10–30 m/s. Qiu et al. [28] simulated the process of grinding IN718 with a single grain by means of 3D finite element simulation (grinding speed ranging from 80 to 1000 m/s). They indicated that the distance between the sawtooth of the grinding chips was reduced when the grinding speed increased from 80 to 240 m/s, and the frequency of adiabatic shear slip increased as the speed was over 400 m/s, resulting in the decline of grinding force, which leads to a more stable machining process. Zhao et al. [29] studied the difference of SQ and chip morphology between different speeds ($20 \le v_s \le 150$ m/s) in single particle grinding IN718 and pointed out that the effect of thermal softening is the main element to decrease both shear slip stress and grinding resistance, which explained the reason why workpiece surface was improved. Accordingly, these works mainly focus on the surface morphology observation after processing, and the analysis of subsurface damage is rarely reported. Meanwhile, the speed range of these studies is wide, and ultra-high-speed machining has not been applied in the current industrial production due to the lack of theory. Therefore, to improve the machining quality of IN718 alloy for the current industrial production and further explain the effect of grinding speed on the workpiece, it is of great significance to explore the effect of grinding speed on its machinability, and comprehensively analyze the relationship between SQ, SSD and machining speed of the ground workpiece.

In this work, as grinding is a common machining approach to prepare the surface of IN718 alloy, we conducted a grinding test with grinding speeds ranging from 5 to 25 m/s to study the SQ and SSD of IN718 alloy. The SQ and SSD of samples at different grinding speeds were characterized and analyzed. Based on the experimental results, the influence mechanism of grinding speed on SQ and SSD was systematically discussed, and the relationship between grinding speed, SQ and SSD was further elaborated.

2 Materials and Methods

2.1 Material

IN718 plate (ASTM B670, solution treatment) was used in the surface grinding experiment. Its chemical composition is shown in Table 1. The microstructure of the as-received IN718 alloy is shown in Figure 1. As shown in Figure 1(a), the matrix is mainly composed of equiaxed grains and secondary phases. Most of the grains are 5–25 μm in diameter and accompanied by a certain number of annealing twins. Typically, the secondary phases in IN718 alloy include δ phase (Ni_3Nb), carbides, and nitrides, meanwhile γ′ phase (Ni_3Al) and γ″ phase (Ni_3Nb) precipitate after aging treatment [30]. In the present work, the needle-like δ phase is observed to distribute along grain boundaries, as indicated by the arrowhead in Figure 1(a). Figure 1(b) and (c) are the energy disperse spectroscopy (EDS) of the grains marked by Spot M and Spot N, respectively. The EDS results imply that they are NbC and TiC, respectively. Nitrides, TiN for

Table 1 Nominal chemical composition of IN718 alloy (wt%)

	Ni	Cr	Fe	Mo	Cu	Al	Ti	Nb	C
Min.	50	17		2.80		0.20	0.65	4.75	
Max.	55	21	Bal.	3.30	0.30	0.80	1.15	5.50	0.08

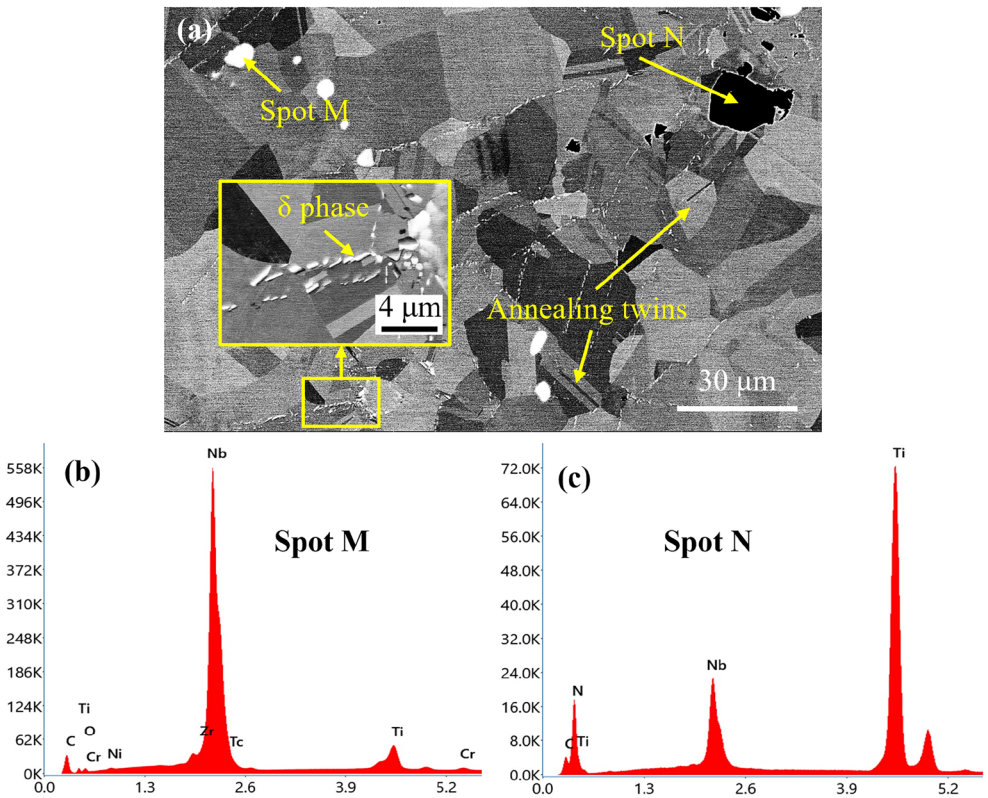

Figure 1 Microstructure of as-received IN718 alloy: (**a**) Scanning electron microscopy (SEM) image, (**b**) and (**c**) EDS confirmation the presence of NbC and TiC

example, are also present in IN718 alloy according to previous work [31]. No tiny γ' and γ'' precipitates could be observed here.

2.2 Grinding Process

A surface grinding test was carried out on the surface grinding machine (MITSUI MSG-618PC-NC). Figure 2 shows the set-up and the schematic diagram of machining process. As shown in Figure 2(a), the IN718 alloy bulk sample was cut into squares (10×10×7 mm) by electrical discharge machining and then was fixed under the ceramic bond CBN grinding wheel (14Al 205×20×31.75×8×10 #80). As the thickness of the abrasive layer is 10 mm, which is bigger than the width of the workpiece—7 mm, thus the entire surface of the workpiece can be ground in a single pass. The upper

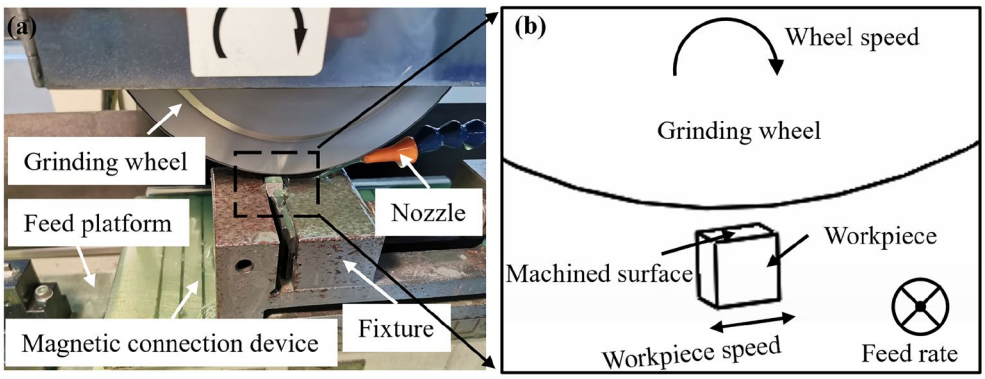

Figure 2 (**a**) Set-up used for the grinding tests, (**b**) Schematic diagram of workpiece processing

surface of the workpiece was ground, as illustrated in Figure 2(b). During the grinding process, a water-based coolant was used to dissipate heat. The grinding parameters were presented in Table 2, and the total grinding depth of each group was set to 420 μm to retain the features induced by the grinding parameters.

2.3 Characterization of Surface Integrity

The physical and mechanical properties of the ground workpiece were mainly investigated by the microhardness tester (HXD-1000TMC/LCD) and nanoindentation tester (KLA, iNano). Among them, the nanoindentation of the subsurface was tested at 6 μm intervals with a 10 mN maximum load. Besides, the change of the lattice parameter was judged by the X-ray diffraction spectrum (XRD, Rigaku Smartlab), which used a wavelength of 1.54178 Å.

The surface finish was measured by a non-contact optical 3D profiler (Taylor Hobson CCI HD), and surface roughness Sa was selected for calibration. In addition, the microstructure was observed using a scanning electron microscope (SEM, FEI, Apreo 2 S) and electron backscattered diffraction (EBSD, EDAX). All EBSD images were scanned with a step size of 0.3 μm, and data points with a confidence index less than 0.1 were deleted during post-processing. The EBSD samples were prepared by grinder with SiC sandpaper of #1000 to #3000, and polished for over 4 h in a vibration polishing machine.

Table 2 Experimental parameters of grinding

Wheel speed v_s (m/s)	Depth of cut a_p (μm)	Workpiece speed v_w (mm/min)	Feed rate f (mm/min)
5, 10, 15, 20, 25	6	120	120

3 Results

3.1 Processing Damage Mechanism

3.1.1 Types of Surface Damage

After the grinding process, several types of surface damage can be observed, including surface tears, breakage of carbide, recasting layer, side flow, material smearing, cavity, ridges and grooves. The typical morphology is shown in Figure 3. The breakage of carbide occurs in all studied velocity ranges. When the abrasive grain touches the upper part of the carbide, the carbide grain cannot be deformed with the matrix material, resulting in breakage. When the abrasive grain touches most of the carbide, it may cause the carbide grain to fall off as a whole, thus leaving a cavity on the ground surface.

3.1.2 Characteristics of Subsurface Damage

As shown in Figure 4(a), the subsurface of the sample after grinding could be divided into three regions: (1) white layer (region A); (2) severe plastic deformation region (region B); (3) matrix (region C). Typically, the

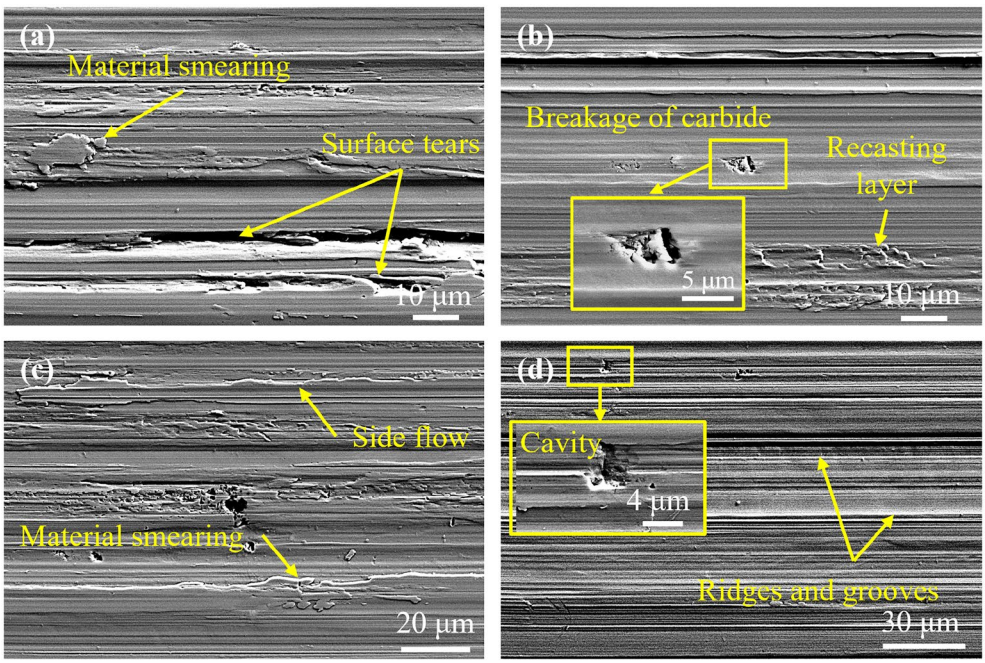

Figure 3 Different types of surface damage: (**a**) Material smearing and surface tears, (**b**) Recasting layer and breakage of carbide, (**c**) Side flow and material smearing, (**d**) Cavity, ridges and grooves

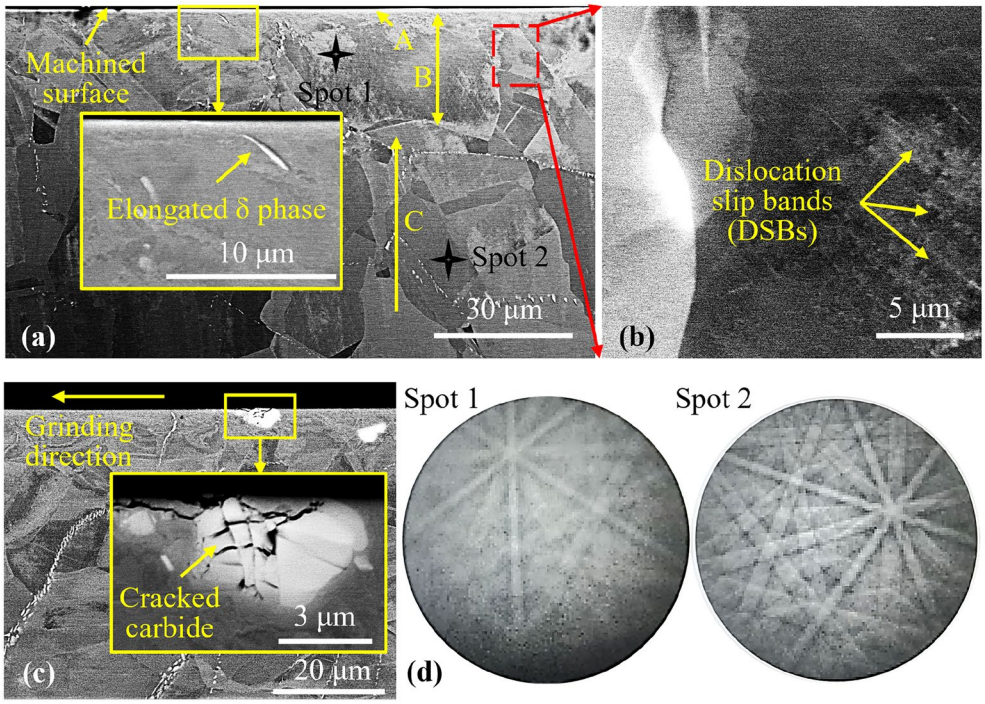

Figure 4 (**a**) Regional division of subsurface, and subsurface features with elongated δ phase and DSBs, (**b**) Magnified image of DSBs, (**c**) Subsurface feature with cracked carbide, (**d**) The Kikuchi patterns of spot 1 and spot 2 from (**a**)

damage of the subsurface is mainly concentrated in the white layer which is characterized by grain refinement, and the severe plastic deformation region where dislocation slip bands (DSBs) aggregate (Figure 4(b)). The features of DSBs are as follows: (1) grains with different orientations have different extension directions of the internal DSBs; (2) The DSBs are distributed in parallel and crisscross. In addition, the Kikuchi pattern corresponding to the processing affected zone and the material matrix is shown in Figure 4(d), respectively. Compared with the Kikuchi pattern of point 2, the pattern of point 1 is twisted. Meanwhile, due to the higher dislocation density and strain distribution, the Kikuchi pattern of spot 1 is more diffused. It is worth pointing out that the DSBs distributed inside grains are not uniform and discontinuous. In the subsequent subsurface characterization process, the entire transverse region of the DSBs is regarded as the main plastic deformation region, that is, there will still be scattered DSBs in the matrix region. For IN718, there are also two typical features of the machined affected zone on the subsurface: the elongated δ phase along the grinding direction and the cracked carbide (Figure 4(a) and (c)). The above features can be used as a qualitative distinction judgment, which can easily and quickly demarcate the subsurface damage area. To quantitatively evaluate the subsurface damage, the EBSD data were further supplemented.

3.2 Surface Quality of IN718 Grinding at Different Speeds

Figure 5 shows the surface topography of samples under different grinding speeds. The overview of the processed surface is arranged in the left column of Figure 5, and the magnified images of the dashed boxed region are arranged in its right column. As shown in the left column of Figure 5, the width and depth of the grooves produced by abrasive grains gradually decrease with increasing grinding speed. There are many material smearing and surface tears on the surface of the sample grinding at 5 m/s, as shown in Figure 5(a2). As the grinding speed increases to 15 m/s, the surface tear almost disappears. At the speed of 25 m/s, the size of the material smearing decreased, and its amount was reduced. However, the breakage of carbide could be occasionally observed in all studied samples, as indicated by the arrowhead in Figure 5(b2).

To quantitatively describe the influence of grinding speed on surface topography, the surface roughness Sa of the processed surface was measured. Figure 6 shows the curve of surface roughness Sa and grinding speed v_s. The error bar refers to the standard deviation of Sa obtained by measuring 30 times. With the increase in grinding speed, surface roughness gradually decreases. As well, the standard deviation in surface roughness also decreases with increasing grinding speed. It is suggested that surface tears and material smearing at low

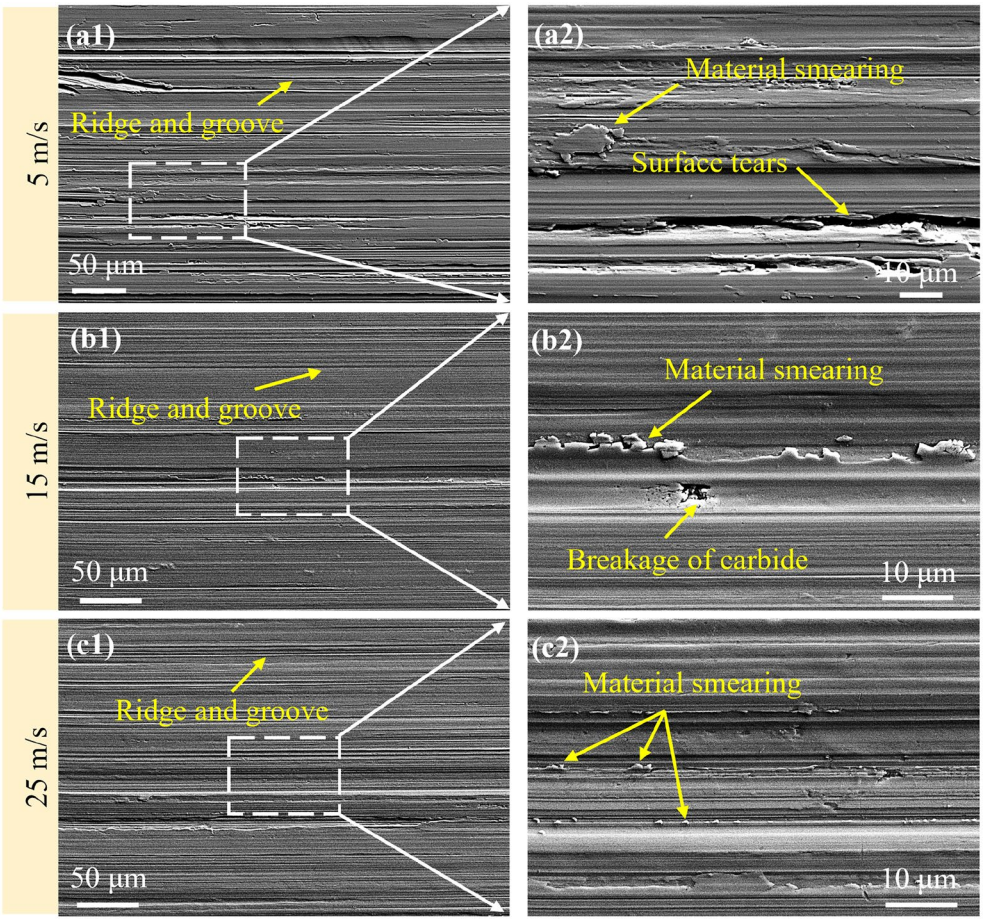

Figure 5 Surface topography of IN718 alloy ground at different grinding speeds: (**a1**) and (**a2**) 5 m/s, (**b1**) and (**b2**) 15 m/s, (**c1**) and (**c2**) 25 m/s

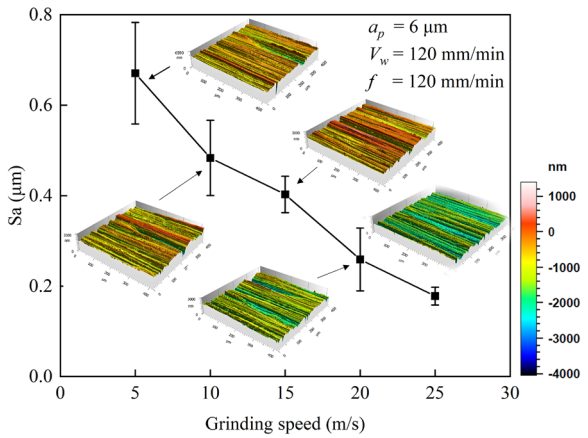

Figure 6 Surface roughness at different grinding speeds

speeds occur more frequently than other forms of damage, and the above two damage types are the major cause in worsening surface roughness. The surface microhardness measurement results are shown in Figure 7. When

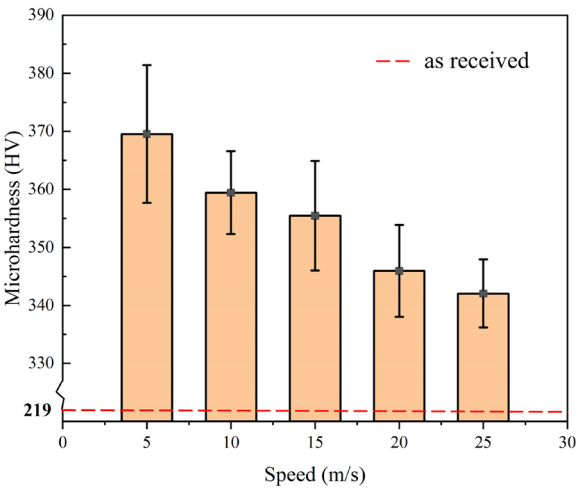

Figure 7 Surface microhardness variation at different grinding speeds

the grinding speed is 5 m/s, the microhardness of the machined surface is relatively large, ranging from 360 to 380 HV. When grinding speed increases to 10–15 m/s, the microhardness decreases to 350–370 HV. As the speed continues to increase, the microhardness declines to 340–350 HV. The decrease in microhardness is mainly due to the alleviation of plastic deformation and the decline of subsurface damage depth.

XRD patterns at different grinding speeds are shown in Figure 8. Figure 8(a) is the composition of diffraction peaks at different grinding speeds, and Figure 8(b)–(d) are the enlarged images of regions I, II and III in Figure 8(a), respectively. As shown in Figure 8(a), all the diffraction peaks of the unprocessed workpiece have a stronger intensity and sharper distribution than those of the processed ones. With increasing grinding speed to 15 m/s, the broadness of the peaks becomes more obvious. As shown in Figure 8(b)–(d), the (111), (200) and (311) peaks of the γ phase in the processed samples shift left relative to those in the unprocessed sample. According to the Bragg's equation, the left shifting of the peaks

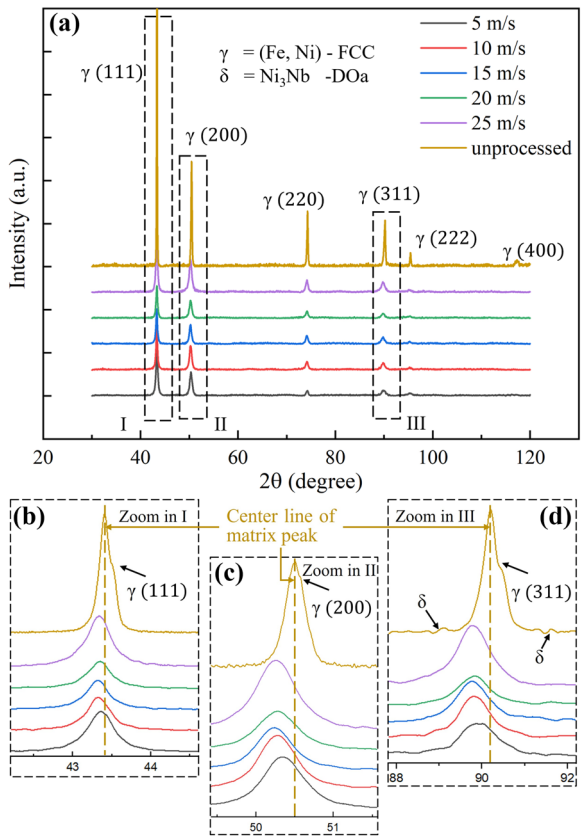

Figure 8 XRD spectrum of the ground surface of IN718 alloy processed at different grinding speeds: (**a**) An overview of all diffraction peaks, (**b**–**d**) Correspond to the magnified image of regions marked by I, II, and III in (**a**), respectively

in a sample with a face-centered cubic (FCC) structure indicates the increase in lattice parameter, reflecting the intensification of plastic deformation. Table 3 summarizes the shift angle of (111), (200) and (311) peaks relative to those in the unprocessed sample. As indicated in Table 3, the absolute value of the angle difference increases as the grinding speed increases to 15 m/s, while it decreases when the grinding speed exceeds 20 m/s. Therefore, it is obvious that the plastic deformation caused by grinding at 15 m/s is more severe than that of other grinding speeds. The lattice constant of the material increases under the action of the residual tensile stress. Generally, the grinding heat mainly leads to residual tensile stress, so it is considered that the heat transferred to the inside of the workpiece increases at the grinding speed of 15 m/s; With the further increase in the speed, the contact time between the workpiece and the abrasive grain is shortened, the heat inside the workpiece reduces, and the degree of plastic deformation alleviates.

3.3 SSD of IN718 Grinding at Different Speeds

3.3.1 Evaluation of SSD Layer

Figure 9 shows the electron channeling contrast (ECC) image of the subsurface of the unprocessed sample and samples grinding at different speeds. The ECC is strongly dependent on the crystal orientation and defects. After deformation, the orientations in a grain become various as the deformation of the grain is heterogenous, leading to a much-blurred contrast compared with that in the well-annealed grain. According to the difference in contrast in the grains close to the surface and deeper depth, the subsurface of the processed samples could be divided into two regions: plastic deformation zone and undeformed matrix. The SSD depth is almost unchanged in the velocity range of 5–15 m/s, then it gradually decreases to 14 and 9 μm when the grinding speed increases up to 20 and 25 m/s, respectively.

To further observe the plastic deformation region, EBSD tests were carried out. The inverse pole figure (IPF) coloring maps of the samples are shown in Figure 10(a)–(e). No obvious grain refinement or change in grain shape was observed near the surface of the samples grinding

Table 3 The shift angle from ground workpiece to unprocessed workpiece

	γ (111) (°)	γ (200) (°)	γ (311) (°)
5 m/s	0.03	0.171	0.24
10 m/s	0.06	0.211	0.28
15 m/s	0.07	0.251	0.37
20 m/s	0.04	0.211	0.22
25 m/s	0.05	0.213	0.29

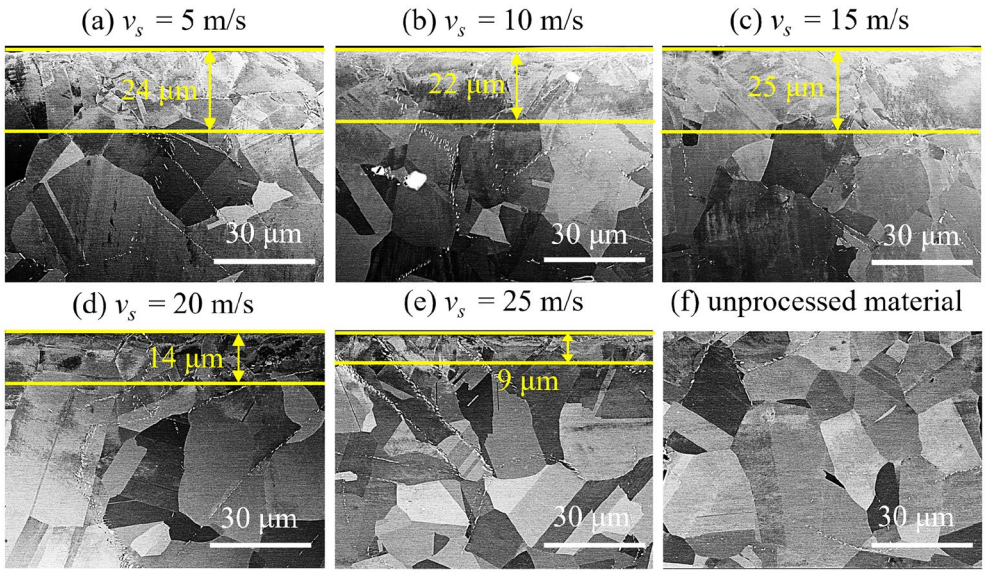

Figure 9 The SSD depth of ground specimens at (**a**) 3 m/s, (**b**) 10 m/s, (**c**) 15 m/s, (**d**) 20 m/s, (**e**) 25 m/s, (**f**) The clear unprocessed material

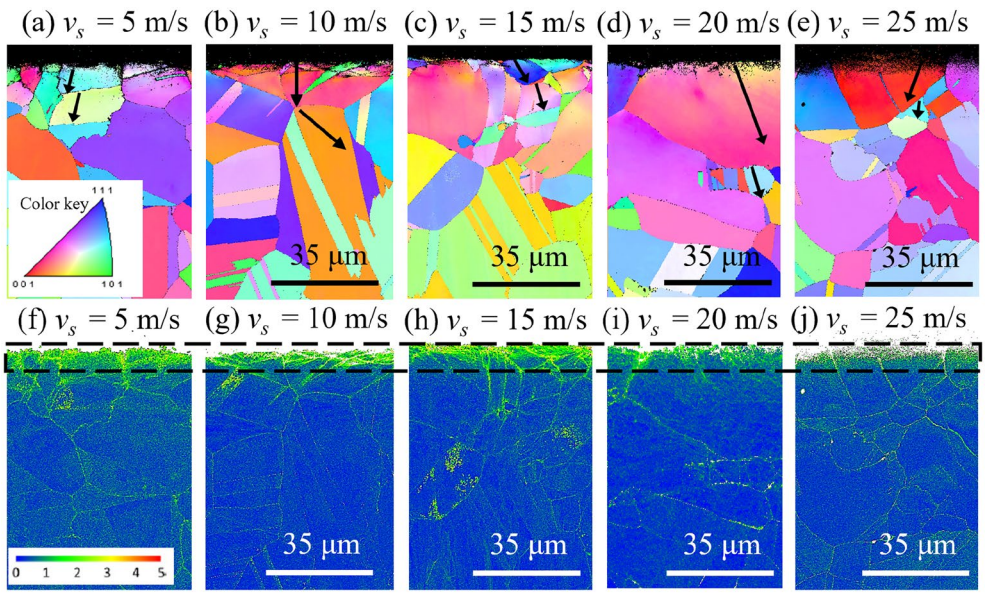

Figure 10 IPF coloring maps of the subsurface processed at different grinding speeds: (**a**) 5 m/s, (**b**) 10 m/s, (**c**) 15 m/s, (**d**) 20 m/s, (**e**) 25 m/s, (**f**–**j**) KAM maps correspond to (**a**–**e**), respectively

up to 25 m/s. The kernel average misorientation (KAM) maps of the samples are shown in Figure 10(f)–(j). The KAM map is established by calculating the misorientation angle between the kernel point with the neighboring points, which is a good indicator of local strain in materials. A higher KAM value indicates a higher local misorientation angle, thus a higher local strain. As shown in Figure 10(f)–(j), the local misorientation angle increases from matrix to surface in all deformed samples, indicating that deformation mainly occurs near the surface. However, the KAM values near the surface in the samples grinding at 20 and 25 m/s are significantly lower than those at 5–15 m/s, demonstrating that the samples grinding with higher speeds experienced a slighter deformation than those with lower speeds.

To further quantify the change of subsurface misorientation, the changes of misorientation angle in the close-to-surface grains and the beneath grain were

measured. As shown in Figure 10(a)–(e), the misorientation was calculated along the black lines with an arrowhead, and the point to origin misorientation profiles are shown in Figure 11(a) (close-to-surface grains) and Figure 11(b) (the beneath grain), respectively. It can be seen that the misorientation along the lines in the beneath grain is significantly lower than that in the close-to-surface grains.

As can be seen from the change of misorientation in the close-to-surface grains of Figure 11(a), the change of misorientation in the speed range of 5–15 m/s is significantly greater than that in the speed range of 20–25 m/s within the same distance, indicating that lattice rotation and plastic deformation in the low-speed zone are more severe. In addition, the change of angle is mainly concentrated in the beginning part, that is, the part of the lattice close to the machined surface has severe torsion, while the part far from the machined surface changes slowly. Moreover, a comparison between the curves of 20 m/s and 25 m/s shows that although grain size at 20 m/s is relatively large (difficult to rotate), the angle change of its misorientation is still much larger than that at 25 m/s, indicating that the effect of grain size on lattice rotation is negligible compared with speed change in this work. In addition, the change of misorientation in the speed range of 5–20 m/s is more than 10°–15°, indicating that high angle grain boundaries have been formed.

For the beneath grain of Figure 11(b), with the increase in grinding speed, the misorientation of the beneath grain in low-speed zone (5–15 m/s) changes slightly, while the misorientation in high-speed zone (20–25 m/s) almost stays the same, with angle change about 1°. Thus, the following conclusions can be drawn: the low-speed zone has heavy and deep damage to workpieces, while the high-speed zone makes light and shallow damage to workpieces.

3.3.2 Nanoindentation

Figure 12 shows the load-depth curves of nanoindentation at different distances from surface and nano hardness profiles under different grinding speeds. The comparative analysis of Figure 12(a) and (e) shows that, under the same loading force, the depth of indenter drop is smaller at the grinding speed of 5 m/s, indicating that the work hardening phenomenon is more serious at the grinding speed of 5 m/s. In order to facilitate observation and analysis, meanwhile minimize the influence of unconventional indentation data influenced by hard phases, nonlinear curve fitting (correlation coefficient R2 between 0.87 and 0.95) was carried out for nanoindentation experimental data at different grinding speeds by least square method, as shown in Figure 12(f). With a distance increase from the machined surface, the measured nano hardness value gradually decreases and eventually tends to be stable, and the near-machined surface presents an obvious work-hardening phenomenon. Meanwhile, nano hardness values tend to be stable first at higher speeds (20 m/s and 25 m/s are around 25 μm), while at lower speeds, especially at 10 m/s and 15 m/s, microhardness values tend to be stable at a larger distance from the surface, indicating that influence area on the subsurface is shallower at high speed. In addition, nano hardness values of the near-machined surface are higher at low speed, and there are more data points larger than 4 GPa, which further indicates that the SSD is more serious at low speed.

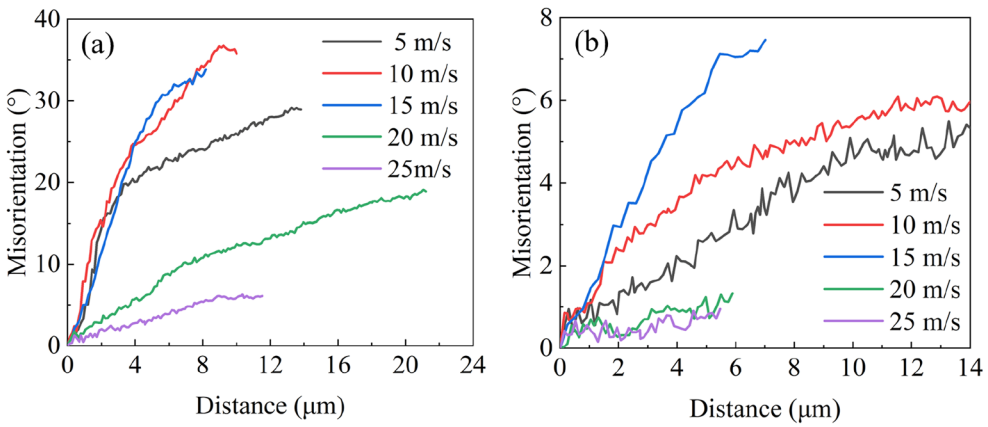

Figure 11 (**a**) The misorientation profiles along depth direction in the close-to-surface grains and (**b**) the beneath grain away from the ground surface

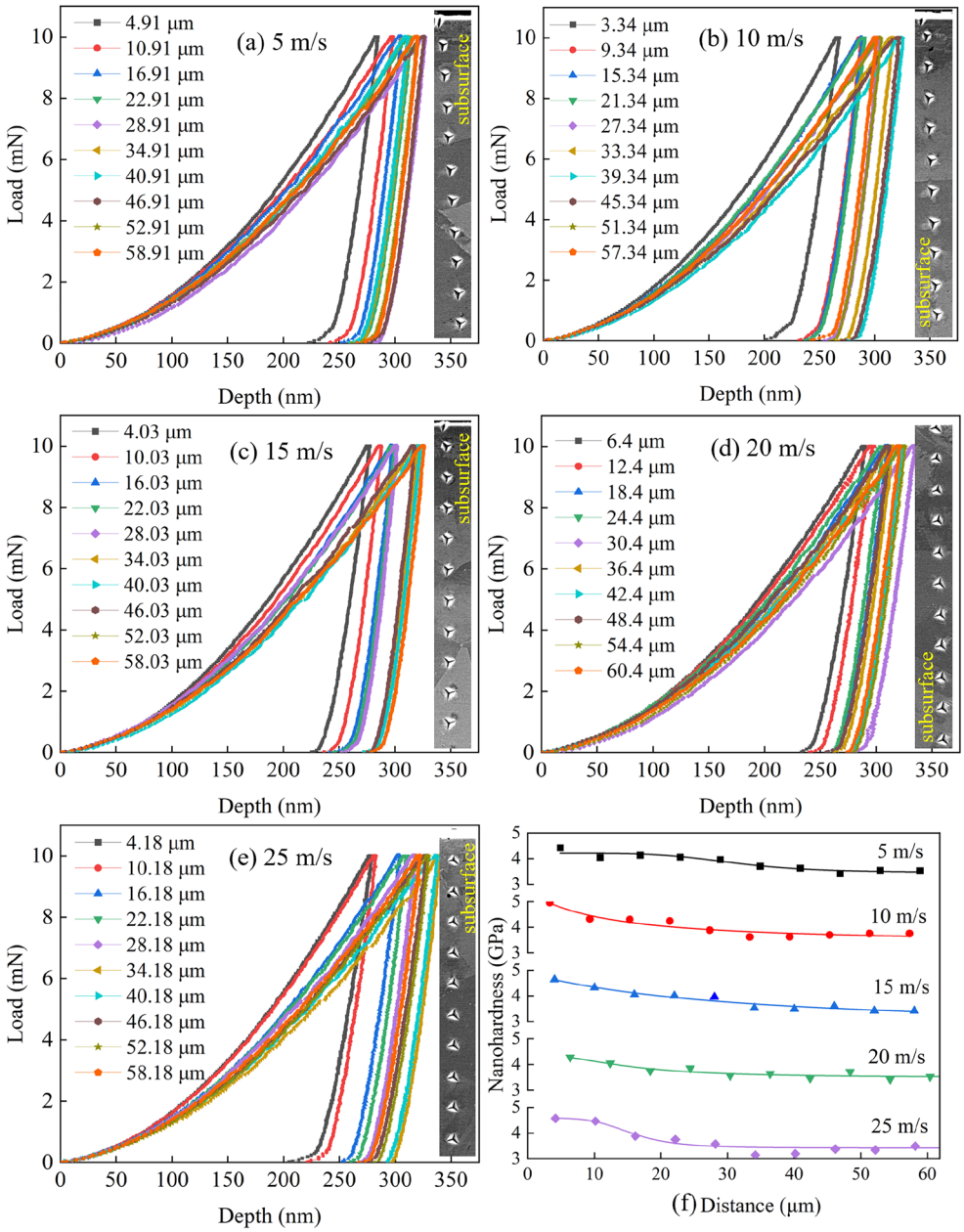

Figure 12 Load-depth curves of nanoindentation at different distances from surface under grinding speed: (**a**) 5 m/s, (**b**) 10 m/s (**c**) 15 m/s, (**d**) 20 m/s, (**e**) 25 m/s, and (**f**) nano hardness profiles below ground surfaces of IN718 at different grinding speeds

4 Discussion

4.1 Analysis of Surface Roughness

Equation (1) is the expression of undeformed chip thickness a_{gmax} in the grinding process [32], where λ represents the average distance between successive and effective abrasive grains, v_w represents the infeed speed of the workpiece, v_s represents the grinding speed, a_p represents the grinding depth, and d_s represents the diameter of the grinding wheel. According to Eq. (1), the undeformed chip thickness decreases with grinding speed, and the effective grinding depth decreases resulting in a reduction in grinding force, thus the SQ of workpieces improves after grinding, which is one of the reasons for the decrease in roughness with the increase in grinding speed.

$$a_{gmax} = 2\lambda \frac{v_w}{v_s} \sqrt{\frac{a_p}{d_s}}. \tag{1}$$

Apart from undeformed chip thickness, the machining damage can also affect surface roughness. Generally, ridges and grooves are damage caused by the grinding process. Breakage of carbide is ascribed to the difference in mechanical properties between hard phase and bulk material. As shown in Figure 5, these two kinds of damage mentioned above are present throughout the studied grinding speed range. However, surface tears and material smearing occur mainly at low speed (5 m/s). The surface tears occur when the material is removed in a tearing state which requires a long interaction time between the material and grinding wheel and high grinding force as well. With the increase in grinding speed (10 m/s and 15 m/s), the size and amount of surface tears and material smearing are reduced. Side flow and recasting layer become the main damage to the machined surface. This is because the material plasticity increases with increasing grinding speed due to the increase of grinding temperature. With further increases in the grinding speed (20 m/s and 25 m/s), the actual interaction time between abrasive grains and the workpiece decreases. On the one hand, the plastic deformation of the workpiece material alleviates (as explained in Figure 8), thus reducing the heat generated by internal friction in the primary deformation zone during the machining process. On the other hand, the heat transferred into the subsurface of the workpiece reduces due to the shortened contact time, resulting in the grinding temperature within the workpiece increasing little or even decreasing [26], thus the phenomenon of side flow and recasting layer is alleviated, and surface roughness is further reduced.

4.2 Subsurface Damage Analysis

SSD is synergistically affected by grinding force and grinding temperature [33, 34]. In the speed range of 5–25 m/s, as the grinding speed increases, the grinding force decreases gradually [29, 35, 36], so the mechanical load acting on the machined surface decreases and plastic deformation of subsurface decreases, leading to a decrease in the depth of the SSD layer. On the other hand, with the increase in grinding speed, material removal speed accelerates, resulting in material deformation is not completely finished, so the actual strain rate of the material decreases (local misorientation value decreases). The degree of plastic deformation is weakened, coupled with the reduction in the depth of subsurface damage, which also explains the decrease in microhardness as grinding speed increases (Figure 7). The accurate measurement of grinding temperature in the machining process itself is a difficult problem due to the uncertainty of the measurement process. In this scenario, the measured temperature cannot accurately reflect the temperature of a certain position inside the workpiece. The influence of grinding temperature discussed here is mainly based on the observed experimental phenomenon. It is noted that in the speed range of 5–15 m/s, the depth of the SSD layer is basically unchanged because the increase in grinding temperature will increase damage to the subsurface. Meanwhile, the SSD depth decreases at 15–25 m/s, implying that the rising trend of the temperature within the workpiece decreases, with the other phenomena including the plastic deformation degree alleviates, and the local misorientation value decreases.

4.3 Relationship between Grinding Speed, Surface Roughness and SSD Depth

The relationship between surface and subsurface should take into account the joint influence of grinding force and grinding temperature. As for the relationship between surface roughness (SR) and subsurface cracks of hard brittle materials, some scholars have given quantitative formulas, which indicate that the SSD of hard brittle materials shows a nonlinear increase trend with the increase of SR [37–41]. For metal and other plastic materials, surface coarsening can be induced by DSBs and grain torsion due to plastic deformation on the subsurface [42], like cracks in hard brittle materials, which belong to the damage caused by processing.

The melting point of hard brittle materials is usually relatively high, so the grinding force is the dominant factor in the relation chain between the surface and subsurface after grinding. However, for plastic materials, the melting point is relatively low, and the dual effects of grinding force and grinding temperature should be considered simultaneously, so the relationship between SQ and SSD is not simply linear. At 5 m/s, it can be seen from Figure 5 that surface tears occupy a large part of material removal at this speed. Under this removal way, significant damage to both surface and subsurface is induced due to the larger grinding force, resulting in a worse SR and a large depth of the SSD layer. With the increase in grinding speed, grinding force in the speed range of 5–15 m/s gradually decreases, but grinding temperature increases. Although the surface roughness in the speed range gradually decreases, the depth of SSD is basically unchanged, attributed to the reduction of grinding force is not conducive to lattice distortion, but the increase in grinding temperature promotes dislocation slip in the material.

In the speed range of 20–25 m/s, with further increase in grinding speed, material removal speed accelerates, thus the material is removed before complete deformation, and the actual strain rate of the material decreases, so the degree of work hardening decreases (Figures 7 and 12). As a result, the grinding force decreases and grinding temperature changes slowly, so both SR and SSD depth decrease (Figures 6 and 10). Therefore, for the speed

range (5–15 m/s) of the grinding temperature increase and the grinding force decrease, the SR decreases with the increase in grinding speed, and the SSD depth does not change much; For the speed range (15–25 m/s) where grinding temperature is almost constant and grinding force decrease, with increase in grinding speed, SR and SSD depth decrease, resulting in 'skin effect' phenomenon [19].

5 Conclusions

The present work emphasizes on the surface integrity of IN718 alloy after grinding with different speeds, and conducts semi-quantitative analysis on processed samples from aspects of work hardening, surface finish, subsurface dislocation slip band, and nanoindentation. Therefore, based on the results and discussion, the following conclusions can be drawn:

(1) With the increase in grinding speed, surface roughness and the degree of work hardening gradually reduce. The SSD depth decreases as a whole.
(2) Under different grinding speeds, the main damage modes of the sample surface are different, which is one of the main reasons for surface quality change. The low-speed region (5 m/s) has a large number of surface tears and material smearing, resulting in the largest surface roughness. With the increase in grinding speed, the number of surface tears and material smearing decreases, thus surface roughness declines.
(3) For the speed range, where grinding temperature and grinding force change inconsistently, the joint influence of grinding force and grinding temperature should be considered for the relationship between surface quality and subsurface damage. In this case, with the increase in grinding speed, surface roughness decreases and subsurface damage depth does not change much. For the speed range where grinding force dominates (grinding temperature does not change much), the surface roughness and SSD depth decrease with the increase in grinding speed.

Acknowledgements
The authors sincerely thanks to Honghai Zhou of Shenzhen Polytechnic University for his help in the surface grinding experiment.

Authors' information
Hao Liu, born in 1995, now is a PhD candidate at *Southern University of Science and Technology, China*. His research interests focus on high-speed machining and molecular dynamics simulation.
Huili Han, a PhD candidate at *Southern University of Science and Technology, China*. Her research interest includes ultrafast laser processing of diamond.
Qinghong Jiang, born in 1995, a PhD candidate at *Southern University of Science and Technology, China*. His research interests include selective laser melting and high-speed machining.
Minglin He is currently a research assistant professor at *Southern University of Science and Technology, China*. Her research interests focus on 3d metal printing and microstructure characterization.
Bi Zhang is currently a chair professor at *Southern University of Science and Technology, China*. His research interests include precision machining, and additive/subtractive hybrid manufacturing.

Authors' Contributions
BZ and HL were in charge of the whole trial; HL wrote the manuscript; HH, QJ, and MH assisted with sampling and laboratory analyses. All authors read and approved the final manuscript.

Funding
Supported by Shenzhen Municipal Science and Technology Innovation Commission of China (Grant Nos. KQTD20190929172505711, JSGG20210420091802007, GJHZ20210705141807023).

Availability of Data and Materials
Not applicable.

Competing Interests
The authors declare no competing financial interests.

Received: 28 April 2023 Revised: 31 January 2024 Accepted: 12 March 2024
Published online: 07 April 2024

References

[1] T Zhu, M Cai, Y Gong, et al. Study on chip formation in grinding of nickel-based polycrystalline superalloy GH4169. *The International Journal of Advanced Manufacturing Technology*, 2022, 121: 1135-1148.
[2] C Liu, M Wan, W Zhang, et al. Chip formation mechanism of Inconel 718: A review of models and approaches. *Chinese Journal of Mechanical Engineering*, 2021, 34: 34.
[3] J W Wang, T Y Yu, W F Ding, et al. Wear evolution and stress distribution of single CBN superabrasive grain in high-speed grinding. *Precision Engineering*, 2018, 54: 70-80.
[4] Z Chen, M H Colliander, G Sundell, et al. Nano-scale characterization of white layer in broached Inconel 718. *Materials Science and Engineering: A*, 2017, 684: 373-384.
[5] T R Newton, S N Melkote, T R Watkins, et al. Investigation of the effect of process parameters on the formation and characteristics of recast layer in wire-EDM of Inconel 718. *Materials Science and Engineering: A*, 2009, 513-514: 208-215.
[6] D Zhu, X Zhang, H Ding. Tool wear characteristics in machining of nickel-based superalloys. *International Journal of Machine Tools and Manufacture*, 2013, 64: 60-77.
[7] A Iturbe, E Giraud, E Hormaetxe, et al. Mechanical characterization and modelling of Inconel 718 material behavior for machining process assessment. *Materials Science and Engineering: A*, 2017, 682: 441-453.
[8] E J Kim, C M Lee. Experimental study on power consumption of laser and induction assisted machining with Inconel 718. *Journal of Manufacturing Processes*, 2020, 59: 411-420.
[9] S H Moon, C M Lee. A study on the machining characteristics using plasma assisted machining of AISI 1045 steel and Inconel 718. *International Journal of Mechanical Sciences*, 2018, 142: 595-602.
[10] Z L Peng, X Y Zhang, D Y Zhang. Performance evaluation of high-speed ultrasonic vibration cutting for improving machinability of Inconel 718 with coated carbide tools. *Tribology International*, 2021, 155: 106766.
[11] D Lu, Q Wang, Y B Wu, et al. Fundamental turning characteristics of Inconel 718 by applying ultrasonic elliptical vibration on the base plane. *Materials and Manufacturing Processes*, 2015, 30(8): 1010-1017.

[12] T Obikawa, M Yamaguchi, K Funai, et al. Air jet assisted machining of nickel-base superalloy. *International Journal of Machine Tools and Manufacture*, 2012, 61: 20-26.
[13] C Courbon, V Sajn, D Kramar, et al. Investigation of machining performance in high pressure jet assisted turning of Inconel 718: A numerical model. *Journal of Materials Processing Technology*, 2011, 211(11): 1834-1851.
[14] Z L Fang, T Obikawa. Turning of Inconel 718 using inserts with cooling channels under high pressure jet coolant assistance. *Journal of Materials Processing Technology*, 2017, 247: 19-28.
[15] F Pusavec, H Hamdi, J Kopac, et al. Surface integrity in cryogenic machining of nickel based alloy-Inconel 718. *Journal of Materials Processing Technology*, 2011, 211(4): 773-783.
[16] L Li, N He, M Wang, et al. High speed cutting of Inconel 718 with coated carbide and ceramic inserts. *Journal of Materials Processing Technology*, 2002, 129(1-3): 127-130.
[17] J Diaz-Alvarez, V Criado, H Miguelez, et al. PCBN performance in high speed finishing turning of Inconel 718. *Metals*, 2018, 8(8): 582.
[18] X Yang, B Zhang. Material embrittlement in high strain-rate loading. *International Journal of Extreme Manufacturing*, 2019, 1(2): 022003.
[19] B Zhang, J Yin. The 'skin effect' of subsurface damage distribution in materials subjected to high-speed machining. *International Journal of Extreme Manufacturing*, 2019, 1(1): 012007.
[20] S Guo, J Zhang, Q Jiang, et al. Surface integrity in high-speed grinding of Al6061T6 alloy. *CIRP Annals*, 2022, 71(1): 281-284.
[21] S Guo, S Lu, B Zhang, et al. Surface integrity and material removal mechanisms in high-speed grinding of Al/SiCp metal matrix composites. *International Journal of Machine Tools and Manufacture*, 2022, 178: 103906.
[22] R M'Saoubi, T Larsson, J Outeiro, et al. Surface integrity analysis of machined Inconel 718 over multiple length scales. *CIRP Annals*, 2012, 61(1): 99-102.
[23] M Imran, P T Mativenga, A Gholinia, et al. Evaluation of surface integrity in micro drilling process for nickel-based superalloy. *International Journal of Advanced Manufacturing Technology*, 2011, 55(5-8): 465-476.
[24] J M Zhou, V Bushlya, J E Stahl. An investigation of surface damage in the high speed turning of Inconel 718 with use of whisker reinforced ceramic tools. *Journal of Materials Processing Technology*, 2012, 212(2): 372-384.
[25] B Wang, Z Liu, Y Cai, et al. Advancements in material removal mechanism and surface integrity of high speed metal cutting: A review. *International Journal of Machine Tools and Manufacture*, 2021, 166: 103744.
[26] C W Dai, W F Ding, Y J Zhu, et al. Grinding temperature and power consumption in high speed grinding of Inconel 718 nickel-based superalloy with a vitrified CBN wheel. *Precision Engineering*, 2018, 52: 192-200.
[27] R D Ruzzi, R L de Paiva, L R R da Silva, et al. Comprehensive study on Inconel 718 surface topography after grinding. *Tribology International*, 2021, 158: 106919.
[28] B Qiu, Y J Zhu, W F Ding. An investigation on material removal mechanism in ultra-high-speed grinding of nickel-based superalloy: Three-dimensional simulation and experimental verification. *International Journal of Advanced Manufacturing Technology*, 2020, 110(3-4): 919-933.
[29] J Y Zhao, Y C Fu, J H Xu, et al. Forces and chip morphology of nickel-based superalloy Inconel 718 during high speed grinding with single grain. *Key Engineering Materials*, 2013, 589-590: 209-214.
[30] H L Qin, Z N Bi, H Y Yu, et al. Influence of stress on gamma " precipitation behavior in Inconel 718 during aging. *Journal of Alloys and Compounds*, 2018, 740: 997-1006.
[31] Q Yin, Z Liu, B Wang, et al. Recent progress of machinability and surface integrity for mechanical machining Inconel 718: a review. *The International Journal of Advanced Manufacturing Technology*, 2020, 109(1-2): 215-245.
[32] S Malkin, C Guo. *Grinding technology: Theory and applications of machining with abrasives*, 2nd edn. New York: Industrial Press, 2008.
[33] H Wang, X G Guo, Z G Dong, et al. Effects of cutting force on formation of subsurface damage during nano-cutting of single-crystal tungsten. *Journal of Manufacturing Science and Engineering*, 2022, 144(11): 111008.
[34] M Papanikolaou, F R Hernandez, K Salonitis. Investigation of the subsurface temperature effects on nanocutting processes via molecular dynamics simulations. *Metals*, 2020, 10(9): 1220.
[35] B K Li, Q Miao, M Li, et al. An investigation on machined surface quality and tool wear during creep feed grinding of powder metallurgy nickel-based superalloy FGH96 with alumina abrasive wheels. *Advances in Manufacturing*, 2020, 8(2): 160-176.
[36] C W Dai, T Y Yu, W F Ding, et al. Single diamond grain cutting-edges morphology effect on grinding mechanism of Inconel 718. *Precision Engineering*, 2019, 55: 119-126.
[37] Z Q Yao, W B Gu, K M Li. Relationship between surface roughness and subsurface crack depth during grinding of optical glass BK7. *Journal of Materials Processing Technology*, 2012, 212(4): 969-976.
[38] J F Yin, Q Bai, S Goel, et al. An analytical model to predict the depth of sub-surface damage for grinding of brittle materials. *CIRP Journal of Manufacturing Science and Technology*, 2021, 33: 454-464.
[39] C Li, F H Zhang, Z K Ma. Study on grinding surface deformation and subsurface damage mechanism of reaction-bonded SiC ceramics. *Proceedings of the Institution of Mechanical Engineers, Part B: Journal of Engineering Manufacture*, 2018, 232(11): 1986-1995.
[40] Y Z Dai, F P Chiang. On the mechanism of plastic-deformation induced surface-roughness. *Journal of Engineering Materials and Technology*, 1992, 114(4): 432-438.
[41] M R Stoudt, J B Hubbard, S D Leigh. On the relationship between deformation-induced surface roughness and plastic strain in AA5052-Is it really linear? *Metallurgical and Materials Transactions A*, 2011, 42(9): 2668-2679.
[42] N Nie, L H Su, G Y Deng, et al. A review on plastic deformation induced surface/interface roughening of sheet metallic materials. *Journal of Materials Research and Technology*, 2021, 15: 6574-6607.